Relationships Between Internal Solitary Wave Surface Features in Optical and SAR Satellite Images: Insights From Remote Sensing and Laboratory

Kexiao Lu[1], Tao Xu[1], Xu Chen[1,2*], Xiao He[1], Yulin Guo[1], and Jiao Tan[1]

[1] Frontiers Science Center for Deep Ocean Multispheres and Earth System and Key Laboratory of Physical Oceanography, Ocean University of China, Qingdao, China.

[2] Laoshan Laboratory, Qingdao, China.

Corresponding author: Xu Chen (chenxu001@ouc.edu.cn)

Key Points:

- The differences and quantitative relationships between internal solitary wave surface features in optical and SAR images were explored
- The laboratory experiments revealed a consistent quantitative relationship with the remote sensing results
- The free surface displacement induced by internal solitary waves was the cause of the difference

Abstract

Internal solitary waves (ISWs) induce convergence and divergence of sea surface currents, manifesting as alternating bright-dark stripes in optical and synthetic aperture radar (SAR) images. Although the relationship between ISWs surface features in SAR images and sea surface currents has been extensively explored, it hasn't been clearly quantified in optical images. This study contrasts surface features of the same ISWs using optical and SAR images with short time intervals, and statistically analyzes the 450 ISW stripe widths determined by the distance between the brightest and darkest points in the image. The results demonstrate that ISW surface features in optical and SAR images differ, with the stripe widths of SAR images being 0.83 times those of optical images. Laboratory experiments simulating surface features in optical and SAR images exhibit a consistent quantitative relationship with remote sensing results, and this difference is primarily attributed to the free surface displacement induced by ISWs.

Plain Language Summary

Internal solitary waves (ISWs) are common mesoscale oceanic phenomena that are widely distributed across the world's oceans. ISWs induce changes in sea surface currents, modulating surface waves and creating rough and smooth regions on the sea surface, which present alternating bright-dark stripes in optical and synthetic aperture radar (SAR) images. The ISW surface features in satellite images are related to the changes in sea surface currents induced by ISWs. This relationship has been extensively explored in SAR images, but it hasn't been clearly quantified in optical images. This study utilizes the bright-dark stripe widths of images to represent the ISW surface features. By comparing the stripe widths of the same ISWs in optical and SAR images, differences in the surface features are revealed, with the stripe widths of SAR images being 0.83 times those of optical images. Laboratory experiments simulating the surface features observed in optical and SAR images demonstrate a consistent quantitative relationship with the remote sensing results. Further experiments reveal that the free surface displacement induced by ISWs is the cause of the differences in the ISW surface features between optical and SAR images. This research provides support for broader quantitative applications of optical remote sensing images.

1 Introduction

Internal solitary waves (ISWs) are nonlinear internal waves that are present throughout many marginal seas and are usually generated due to the nonlinear steepening of internal tides (Ramp et al., 2010). These waves are characterized by large amplitudes (Huang et al., 2016), short periods, and high velocities. ISWs have an important impact on material transport (Dong et al., 2015; Schafstall et al., 2010), vertical mixing (Shroyer et al., 2010; Xu et al., 2012), underwater acoustic transmission (Badiey et al., 2013; Duda et al., 2019) and the safety of underwater vehicles (Gong et al., 2022; Wang et al., 2022) in the ocean.

As ISWs propagate through the ocean, they modulate the redistribution of microscale waves on the sea surface, thereby changing the distribution of sea surface roughness, and thus can be observed by satellite remote sensing. With the rapid development of satellite and sensor technology, a large amount of satellite remote sensing data has been generated that can be used to study the ISW spatiotemporal distribution (Sun et al., 2019; Wang et al., 2011), sources of generation (Liang et al., 2022; Raju et al., 2019), and propagation evolution (Gao et al., 2018; Sun et al., 2021) and reveal their interactions with the surrounding topography (Li et al., 2013; Zhao et al., 2008). Compared with SAR remote sensing, optical remote sensing comes with the advantages of high temporal resolution (Vanhellemont et al., 2014) and extensive spatial coverage (Jackson, 2007), allowing for real-time observations of ISWs across global ocean regions. Consequently, the widespread application of optical remote sensing images can provide more data support for propagation evolution, in-situ data matching and prediction research on ISWs.

The mechanism of remote sensing imaging is the basis of ISW remote sensing research, and the imaging mechanisms vary among different remote sensing images. ISWs become visible on SAR images because the convergence and divergence of sea surface currents induced by ISWs modulate the surface wave spectrum and thus the normalized radar cross section (Alpers, 1985). The relationships between the ISW surface features in SAR images and sea surface currents have been widely applied (Chen et al., 2011; Jia et al., 2019; Zheng et al., 2001). For optical images, the imaging of ISWs is mainly due to the fact that ISWs modulate the surface roughness which in turn modulates the sun glitter (the specular reflection of sunlight by suitably tilted facets of the water surface into the sensor) pattern of the sea surface (Melsheimer & Keong, 2001). If the imaging geometry (i.e., the sun's position in the sky, the sensor's viewing direction)

is suitable, ISWs can be observed in optical images (Jackson & Alpers, 2010). The signals received by optical sensors are affected by wind speed (Cox & Munk, 1954), imaging geometry (Jackson & Alpers, 2010), and cloud cover or aerosols. Consequently, it is difficult for the ISW surface features in optical images to clearly and quantitatively represent the changes in sea surface currents induced by ISWs.

The short revisit period of optical remote sensing makes it possible to find the same ISW observed simultaneously by optical and SAR remote sensing images, allowing for exploration of the differences in ISW surface features between optical and SAR images. Moreover, laboratory experiments can simulate optical remote sensing imaging (Mei et al., 2019; Zhang et al., 2022) and measure the surface velocity divergence corresponding to SAR remote sensing surface features (Xu et al., 2023) to further investigate discrepancies in the ISW surface features. Therefore, this study uses satellite remote sensing and laboratory experiments to explore the differences and reasons for the ISW surface features in optical and SAR images and to determine the quantitative relationship of the differences between the two. It is helpful to explore the relationship between the ISW surface features in optical images and sea surface currents and can better explain the optical remote sensing imaging mechanism of ISWs, which is crucial for the more quantitative application of optical images.

The structure of the article is as follows: Section 2 introduces the methods used to extract the ISW surface features in remote sensing images and the setup along with the technical methods used for laboratory experiments. Section 3 presents the results of remote sensing images and laboratory experiments. Section 4 discusses the reasons for the differences in the ISW surface features, and Section 5 summarizes the full text.

2 Methodology

2.1 Satellite Remote Sensing

This study uses satellite remote sensing technology to collect optical and SAR remote sensing images containing the same ISWs at similar times (see Figure S1 in the Supporting Information S1). The optical remote sensing images include MODIS images with a spatial resolution of 250 m and a swath width of 2330 km, and the SAR images include ASAR images (in wide swath mode) with a spatial resolution of 150 m and a swath width of 400 km. MODIS and SAR images were collected from 2003 to 2011 in the northern South China Sea and the

Andaman Sea, and 14 pairs of MODIS and SAR images containing the same ISW features were screened out; see Table S1 in the Supporting Information S1 for a detailed data list. Grayscale profiles perpendicular to the ISW crest are extracted from satellite remote sensing images, and the bright or dark stripes on satellite images manifest as positive or negative peaks on the profile. The distance between the positive and negative peaks, i.e., the peak-to-peak (PP) distance, can be extracted from the grayscale profile. In satellite images, the PP distance of ISWs is less affected by winds in most cases than the signal intensity (Xue et al., 2013) and is related to the characteristic half width of ISWs (Zheng et al., 2001). Therefore, the grayscale profile and PP distance are chosen to represent the ISW surface features in remote sensing images.

All the remote sensing images were preprocessed for geometric correction and image enhancement using the environment for visualizing images software (Meng et al., 2022). Due to the large amount of coherent speckle noise in SAR images, the images are further processed by Lee filtering (Lee, 1980). Depression-type ISWs manifest as bright and dark stripes, where bright stripes are usually easier to recognize in SAR images. By analyzing the image intensity of the ISW crest line and its surroundings, we can identify the brightest points of the image intensity (the red points in Figure 1a), determine the bright stripe and propagation direction of ISWs (the black arrow in Figure 1a), and then extract the grayscale profile of ISWs in reverse (Figure 1c).

After overlaying the MODIS images with the SAR images (Figure 1a), the corresponding positions of the ISWs in the MODIS image are determined along the propagation direction of the ISWs in the SAR image. By applying the same method as for the SAR images, the dark stripe of ISWs in the MODIS image (the blue points in Figure 1a) is identified, thereby extracting the grayscale profile of the ISWs in the MODIS image (Figure 1b). The difference in the distance between the brightest and darkest points on the grayscale profile is the PP distance, which can be expressed as

$$D_{p-p} = \left| x_{|\max(Gray)} - x_{|\min(Gray)} \right|. \quad (1)$$

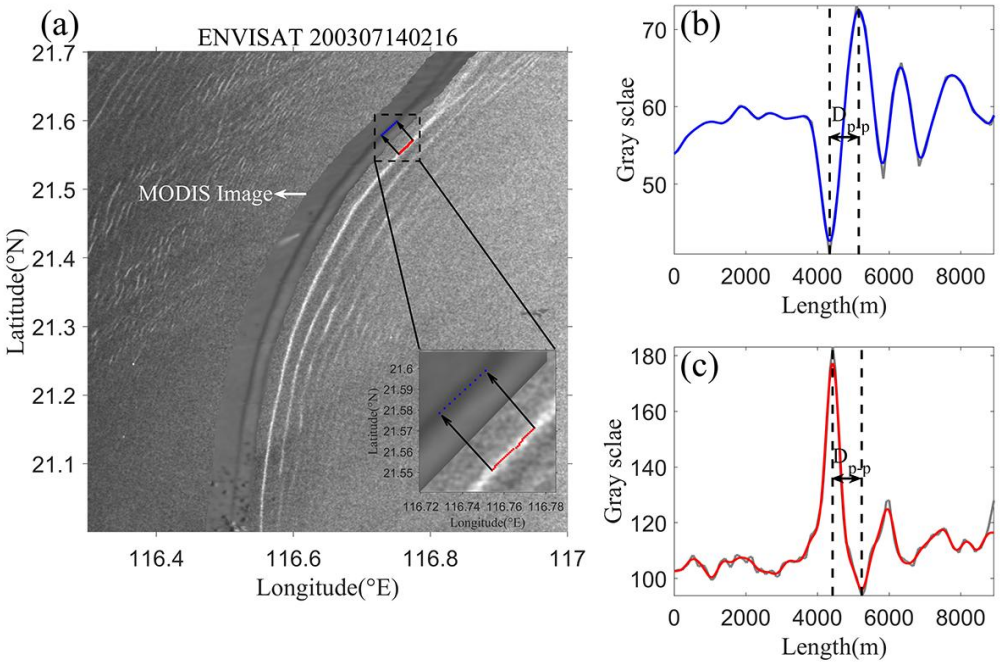

Figure 1. (a) Overlay image of SAR and MODIS; the SAR image was acquired at 02:16:23 UTC on July 14, 2003, and the MODIS image was acquired at 03:00:00 UTC on July 14, 2003. The insert is a magnified view within the black dashed box. The blue points are the darkest points of the MODIS image, the red points are the brightest points of the SAR image, and the black arrow is the propagation direction of the ISWs. (b) The average of all blue point grayscale profiles in the MODIS image; the gray and blue lines represent the original and low-pass filtered results, respectively. (c) The average of all the red point grayscale profiles in the SAR image; the gray and red lines represent the original and low-pass filtered results, respectively. The black dashed lines in (b) and (c) indicate the horizontal positions corresponding to the maximum and minimum values, respectively.

2.2 Laboratory Experiments

To investigate the differences in the ISW surface features between optical and SAR images and their causes, we established an experimental system for simultaneously observing ISWs using optical and particle image velocimetry (PIV) in the laboratory (a schematic diagram is shown in Figure 2a). The tank is 6 m long, 0.25 m wide, and 0.5 m tall, where two layers of fluid with thicknesses of h_1 (upper layer) and h_2 (lower layer) and densities of 1020 kg/m^3 and 1060 kg/m^3 are injected, respectively. The depth ratio of the lower and upper layers h_2/h_1 varies

from 3 to 9. The non-dimensional amplitudes (amplitudes/upper layer) ranged from 0.24 to 2.42, see Table S2 in the Supporting Information S1 for detailed conditions.

The ISWs are generated by the gravity collapse method (Kao et al., 1985) using a movable gate of the same width as the tank. A plane light source is positioned at the upper right side of the tank instead of the sun as the radiation source. On the left side, a charge coupled device (CCD) camera serves as an optical imaging sensor to record optical images of the surface. The fluid is seeded with 40-μm-diameter tracer particles made of polystyrene and illuminated by a laser (532 nm). The wave-induced velocity is measured by the particle image velocity (PIV) (Thielicke & Stamhuis, 2014) (see Figure S2 in the Supporting Information S1). Another CCD camera is placed in front of the tank to record the PIV images. Both CCDs record at a frequency of 40 Hz. Considering the geometric angle of ISWs in MODIS images and the observation limitations in the laboratory, the zenith angles of the sensor and the light source are set to 13.54° and 17.62°, respectively, and the relative azimuth angle is 180°.

Figure 2b is the surface grayscale image recorded by CCD1, showing the dark and bright stripes on the surface caused by ISWs. The grayscale profile (Figure 2c) is obtained from the grayscale image, and then the ISW PP distance of the optical image in the laboratory is calculated. Combining the weak hydrodynamic interaction theory and Bragg scattering theory, the relationship between the normalized radar cross section (NRCS) in SAR images and surface currents can be written as (Alpers, 1985; Jackson et al., 2013)

$$\frac{\Delta\sigma}{\sigma_0} = -A\frac{\partial u_x}{\partial x}, \tag{2}$$

where $\Delta\sigma = \sigma - \sigma_0$ denotes the deviation of the NRCS intensity from its background value. A is a constant that depends on the radar wavelength, incidence angle, and relaxation rate. u_x denotes the velocities of surface currents (Figure 2d). This means that the PP distance of ISWs in SAR images can be calculated from the divergence of surface velocities (Figure 2e) in the laboratory. The PP distance of the SAR image in the experiment is expressed as

$$D_{p-p} = \left| T_{\left|\max\left(\frac{\partial u_x}{\partial x}\right)} - T_{\left|\min\left(\frac{\partial u_x}{\partial x}\right)} \right| * C. \tag{3}$$

where C denotes the propagation speed of ISWs.

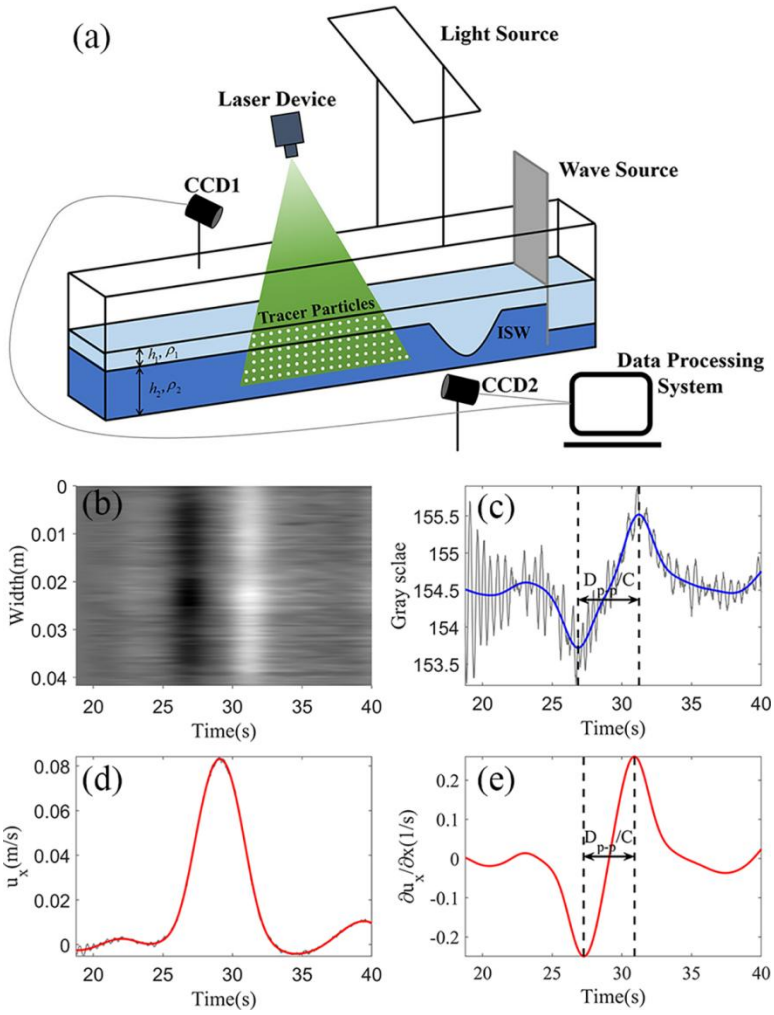

Figure 2. (a) Schematic diagram of the laboratory platform. (b) Optical surface grayscale image recorded by CCD1. (c) Optical grayscale profile curve; the gray and blue lines represent the original and low-pass filtered results, respectively. (d) Surface horizontal velocity curve; the gray and red lines represent the original and low-pass filtered results, respectively. (e) Surface horizontal velocity divergence curve. The black dashed lines in (c) and (e) indicate the times corresponding to the maximum and minimum values, respectively.

3 Results

This study analyzes 14 pairs of MODIS and SAR images with the same ISW features in the northern South China Sea and the Andaman Sea. The undulating topography and the obvious vertical stratification structure of seawater produce frequent ISW activity in these regions. Depths vary widely, ranging from several hundred to several thousand meters, and different

depths exhibit distinct stratification conditions, leading to variations in ISW characteristics. Within the depth range of 110 to 1800 m, we extracted grayscale profiles and PP distances of 450 segment ISWs (see Figure S3 in the Supporting Information S1) to explore the differences in surface features of the same ISWs on optical and SAR remote sensing images and the quantitative relationship.

The grayscale profiles of the same ISWs on the MODIS and SAR images are normalized. Taking the middle point between the brightest and darkest points of the grayscale profiles as the corresponding point, the grayscale profiles of ISWs on different images are contrasted and analyzed, as shown in Figures 3a, 3c, and 3e. A comparison of the other grayscale profiles is shown in Figure S4 in Supporting Information S1. The figures show that the fluctuation trends of the grayscale values for the same ISWs are generally consistent between the optical and SAR remote sensing images, but there are differences in the positions corresponding to the brightest and darkest points. This discrepancy arises from the differing optical and SAR remote sensing imaging mechanisms. In the optical images, the grayscale values represent the intensity of the sun glitter radiation received by the sensor (Melsheimer & Keong, 2001; Jackson & Alpers, 2010), which is determined by the surface roughness and the viewing geometry of the image (Cox & Munk, 1954). In SAR images, the grayscale values represent the radar backscatter intensity from the sea surface (Alpers, 1985), which is influenced by the interaction between radar waves and microscale waves on the sea surface. Microscale waves are formed by surface waves modulated through the convergence and divergence of sea surface currents induced by ISWs. The differences in the ISW surface features between optical and SAR remote sensing images indicate that the surface roughness influencing the grayscale values of optical images is affected not only by the convergence and divergence of sea surface currents but also by other phenomena.

In Figures 3a, 3c, and 3e, the symmetries of the bright and dark stripes in the optical images are superior to those in the SAR images. This is because the wind over the sea surface significantly affects the imaging of ISWs in SAR images (Brandt et al., 1999; Quyang et al., 2011). When the wind speed is high, the symmetry of bright and dark stripes in SAR images is poorer than that in optical images. The bright and dark stripes are crucial elements in retrieving dynamic characteristics in the ocean interior from the ISW surface features in remote sensing images (Pan et al., 2007; Romeiser & Graber, 2015). Therefore, when remote sensing images are

used to retrieve ISW wave parameters, optical images with better symmetry of bright and dark stripes are more accurate for inversion than are SAR images.

The PP distance can be extracted from the grayscale profile of ISWs. Figure 4a shows the distribution of PP distances extracted from 450 segments of ISWs in MODIS and SAR remote sensing images, along with their fitted curves. The distribution of PP distances indicates that the PP distances of the same ISWs on the MODIS images are greater than those on the SAR images, and this difference shows a positive correlation. Fitting the PP distances revealed that the PP distances on the SAR images were 0.83 times those on the MODIS images.

Laboratory experiments were conducted to investigate the differences in the ISW surface features in optical and SAR images. We conduct 35 sets of experiments to simulate ISW propagation across depth ratios ranging from 3 to 9 and non-dimensional amplitudes ranging from 0.24 to 2.42. Optical grayscale profiles of the ISW surface, surface horizontal velocity divergence, along with their corresponding PP distances were extracted. Figures 3b, 3d, and 3f show the contrastive analysis of the normalized experimental optical surface grayscale profile and surface horizontal velocity divergence curve under different stratifications and similar non-dimensional amplitudes. The comparison results under the other stratifications are shown in Figure S5 in Supporting Information S1. It can be seen from the results that the surface grayscale profiles and surface horizontal velocity divergence curves are basically consistent for different stratifications, but the positions of their positive and negative peaks are different. This difference is similar to the difference observed in the grayscale profiles obtained from optical and SAR remote sensing images.

Figure 4b displays the distribution of PP distances and the fitting curves for optical surface grayscale profiles and surface horizontal velocity divergence under different stratifications and amplitudes in laboratory experiments. The distribution of the PP distances reveals that the PP distances of the ISWs in the optical grayscale profiles are consistently greater than those of the surface horizontal velocity divergence, regardless of the variations in stratification and amplitude. The fitted curve of the PP distances indicates that the PP distances of the surface horizontal velocity divergence are 0.86 times those of the optical surface, which is similar to the fitting results of the PP distances previously observed in MODIS and SAR remote sensing images.

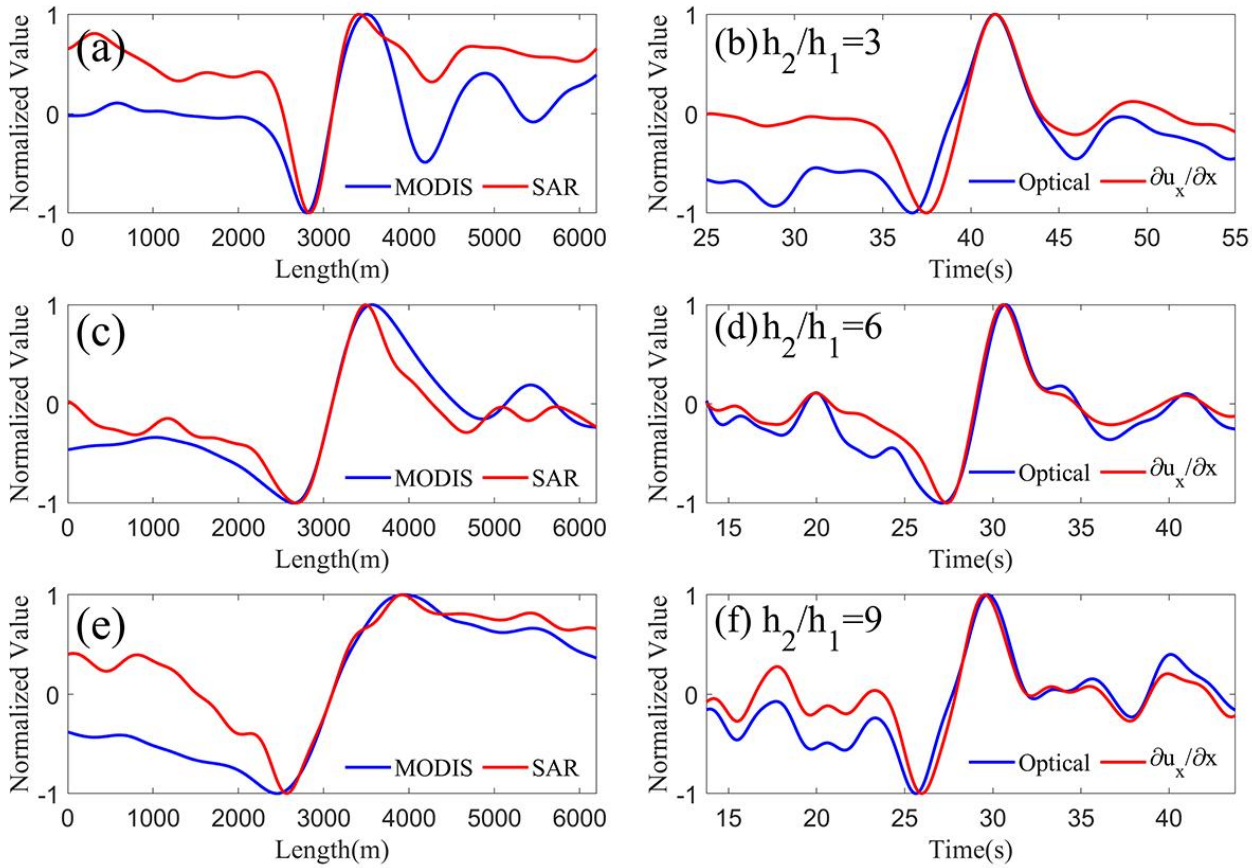

Figure 3. Panels (a), (c), and (e) are grayscale profile comparisons analysis of the same ISW on MODIS and SAR remote sensing images at different PP distances. The blue curve is the grayscale profile of the MODIS image, and the red curve is the grayscale profile of the SAR image. In (a), (c) and (e), the PP distances of ISWs for the MODIS images are 704, 920 and 1493 m, respectively, and the PP distances of ISWs in the SAR images are 579, 810 and 1351 m, respectively. Panels (b), (d), and (f) show a comparison analysis of the experimental optical surface grayscale profile and surface horizontal velocity divergence at different depth ratios and similar non-dimensional amplitudes. The blue curve is the grayscale profile of the experimental optical surface, and the red curve is the surface horizontal velocity divergence.

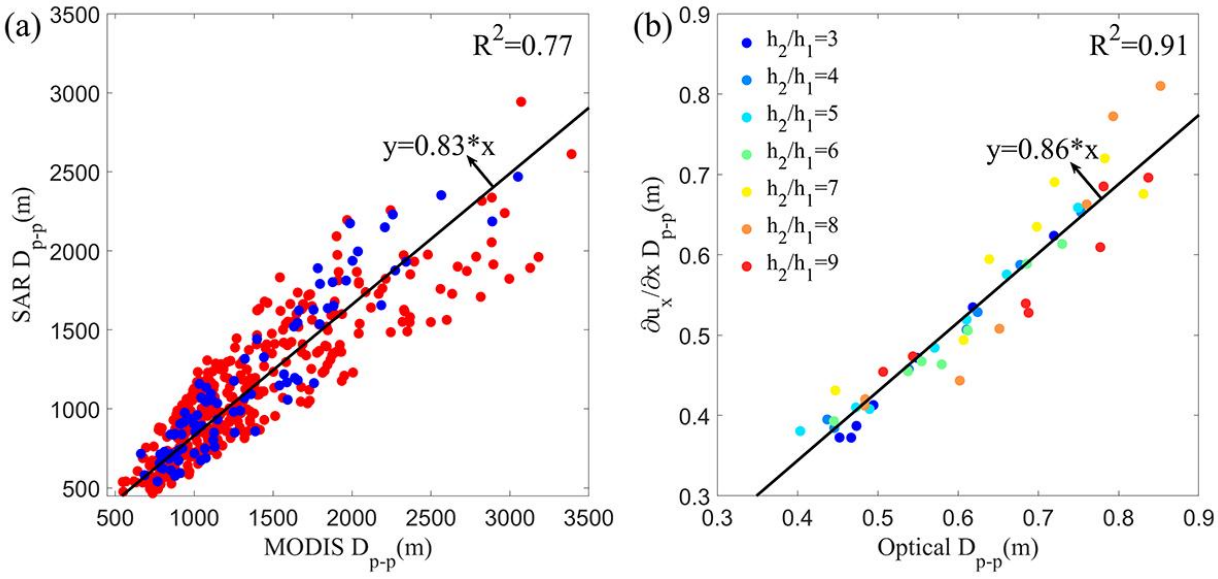

Figure 4. (a) The distribution and fitting curves of the PP distance for the same ISWs on the MODIS and SAR remote sensing images; the red dots are the PP distance data of the South China Sea, with a total of 363 segments of ISW data, and the blue dots are the PP distance data of the Andaman Sea, with a total of 87 segments of ISW data. (b) The distribution and fitting curves of the PP distances for surface optical grayscale profiles and surface horizontal velocity divergence under different depth ratios and amplitudes in the laboratory; different colors represent different depth ratios.

4 Discussion

Previous satellite remote sensing observations have revealed differences in the ISW surface features between optical and SAR images, with the PP distances of SAR images being 0.83 times those of MODIS images. To investigate the reasons for the differences in the ISW surface features between optical and SAR images, we conducted 7 sets of experiments in the laboratory to study the free surface displacement and surface horizontal velocity. The densities of the upper and lower fluids are 1020 kg/m^3 and 1060 kg/m^3, the depth ratios are 5 and 7, and the non-dimensional amplitudes range from 1.06 to 1.77.

Figure 5a illustrates the free surface displacement induced by ISWs, while Figure 5b shows the variation in the pycnocline. As shown in Figure 5a, the leading edge of the ISW wave exhibits significant roughness, whereas the trailing edge appears smoother, which is attributed to the phenomena of convergence and divergence induced by ISWs. The free surface displacement gradient and the surface horizontal velocity divergence are normalized and compared in Figure

5c. The figure shows that the positions of the positive and negative peaks positions of the free surface displacement gradient differ from those of the surface horizontal velocity divergence. Figure 5d presents a comparison between the optical surface grayscale profile and surface horizontal velocity divergence under the same depth ratio and similar non-dimensional amplitude as presented in Figure 5c in the Section 3 experiments. A comparison between Figure 5c and 5d indicates that the differences in the free surface displacement gradient and surface horizontal velocity divergence are similar to the differences observed in the optical surface grayscale profile and surface horizontal velocity divergence. The other comparison results are shown in Figure S6 in Supporting Information S1.

Figure 5e shows the PP distance distribution and data curve fit of the free surface displacement gradient and surface horizontal velocity divergence. The PP distances of the free surface displacement gradient are consistently larger than the surface horizontal velocity divergence. Additionally, the PP distances of the surface horizontal velocity divergence are 0.86 times those of the free surface displacement gradient, which is consistent with the fitting relationship between the optical grayscale profile and surface horizontal velocity divergence in the Section 3 experiment. Therefore, the free surface displacement induced by ISWs affects optical remote sensing imaging, leading to differences in ISW surface features between optical and SAR remote sensing.

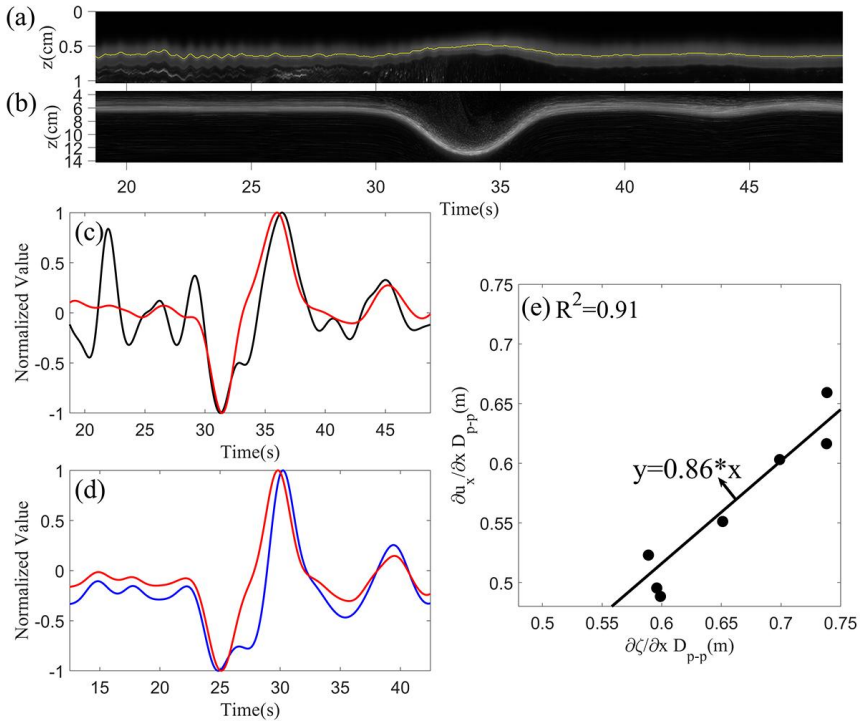

Figure 5. (a) Free surface displacement induced by ISWs. (b) The variation in the pycnocline. (c) Comparison of the free surface displacement gradient and surface horizontal velocity dispersion for a depth ratio of 5 and a dimensionless amplitude of 1.64; the black curve is the free surface displacement gradient, and the red curve is the surface horizontal velocity divergence. (d) Comparison of the optical surface grayscale profile and surface horizontal velocity divergence for a depth ratio of 5; the dimensionless amplitude is 1.62, the blue curve is the grayscale profile of the optical surface, and the red curve is the surface horizontal velocity divergence. (e) The PP distance distribution and curve fit of the free surface displacement gradient and surface horizontal velocity divergence for depth ratios of 5 and 7.

5 Conclusions

In this study, we explore the differences in the ISW surface features between optical and SAR images and their causes using satellite remote sensing and laboratory experiments. The remote sensing results show that the corresponding positions of the brightest and darkest points in the ISW grayscale profile between optical and SAR images are different, and the PP distances of SAR images are 0.83 times greater than those of optical images. Laboratory experiments reveal differences in the positions of the positive and negative peaks between the optical grayscale profile and surface horizontal velocity divergence of ISWs, with the PP distances of surface horizontal velocity divergence being 0.86 times those of the optical grayscale profile. The experimental and remote sensing results are similar. Additional experiments further demonstrate that the PP distances for horizontal velocity divergence on the surface of ISWs are also 0.86 times those of the free surface displacement gradient. This finding suggests that the free surface displacement induced by ISWs affects optical remote sensing imaging, leading to differences in the ISW surface features between optical and SAR remote sensing images.

The surface features extracted from remote sensing images can be used to retrieve the internal structure of ISWs in the ocean (Chen et al., 2011; Jia et al., 2019; Pan et al., 2007; Romeiser & Graber, 2015; Zheng et al., 2001). This work provides statistical support for the quantitative inversion of optical remote sensing images. The inversion of ISW wave parameters using optical images with high spatial and temporal resolution enables a comprehensive understanding of the internal characteristics of ISWs across the whole region and estimates the energy of ISWs. This is crucial for the energy transfer, three-dimensional observation, and

forecasting of ISWs. Further research will include wide-scale inversion of ISW wave parameters using optical remote sensing images in a specific area.

Acknowledgments

The study was supported by the National Natural Science Foundation of China through grant 41876015 and the National Key Research and Development Program of China through grant 2021YFC3101603.

Open Research

The data set of satellite image and laboratory experiments is available at Lu (2024).

References

Alpers, W. (1985). Theory of radar imaging of internal waves. *Nature*, *314*(6008), 245-247. https://doi.org/10.1038/314245a0

Badiey, M., Wan, L., & Song, A. (2013). Three-dimensional mapping of evolving internal waves during the Shallow Water 2006 experiment. *The Journal of the Acoustical Society of America*, *134*(1), EL7-EL13. https://doi.org/10.1121/1.4804945

Brandt, P., Romeiser, R., & Rubino, A. (1999). On the determination of characteristics of the interior ocean dynamics from radar signatures of internal solitary waves. *Journal of Geophysical Research: Oceans*, *104*(C12), 30039-30045. https://doi.org/10.1029/1999jc900092

Chen, G.-Y., Su, F.-C., Wang, C.-M., Liu, C.-T., & Tseng, R.-S. (2011). Derivation of internal solitary wave amplitude in the South China Sea deep basin from satellite images. *Journal of Oceanography*, *67*(6), 689-697. https://doi.org/10.1007/s10872-011-0073-9

Cox, C., & Munk, W. (1954). Measurement of the Roughness of the Sea Surface from Photographs of the Sun's Glitter. *Journal of the Optical Society of America*, *44*(11), 838-850. https://doi.org/10.1364/josa.44.000838

Dong, J., Zhao, W., Chen, H., Meng, Z., Shi, X., & Tian, J. (2015). Asymmetry of internal waves and its effects on the ecological environment observed in the northern South China Sea. *Deep Sea Research Part I: Oceanographic Research Papers*, *98*, 94-101. https://doi.org/10.1016/j.dsr.2015.01.003

Duda, T. F., Lin, Y., Newhall, A. E., Helfrich, K. R., Lynch, J. F., Zhang, W. G., et al. (2019). Multiscale multiphysics data-informed modeling for three-dimensional ocean acoustic simulation and prediction. *The Journal of the Acoustical Society of America*, *146*(3), 1996-2015. https://doi.org/10.1121/1.5126012

Gao, Q., Dong, D., Yang, X., Husi, L., & Shang, H. (2018). Himawari-8 geostationary satellite observation of the internal solitary waves in the South China Sea. *The International Archives of the Photogrammetry, Remote Sensing and Spatial Information Sciences*, *42*, 363-370. https://doi.org/10.5194/isprs-archives-XLII-3-363-2018

Gong, Y., Xie, J., Xu, J., Chen, Z., He, Y., & Cai, S. (2021). Oceanic internal solitary waves at the Indonesian submarine wreckage site. *Acta Oceanologica Sinica*, *41*(3), 109-113. https://doi.org/10.1007/s13131-021-1893-0

Huang, X., Chen, Z., Zhao, W., Zhang, Z., Zhou, C., Yang, Q., & Tian, J. (2016). An extreme internal solitary wave event observed in the northern South China Sea. *Scientific Reports*, *6*, 30041. https://doi.org/10.1038/srep30041

Jackson, C. (2007). Internal wave detection using the Moderate Resolution Imaging Spectroradiometer (MODIS). *Journal of Geophysical Research*, *112*(C11). https://doi.org/10.1029/2007jc004220

Jackson, C., & Alpers, W. (2010). The role of the critical angle in brightness reversals on sunglint images of the sea surface. *Journal of Geophysical Research: Oceans*, *115*(C9). https://doi.org/10.1029/2009JC006037

Jackson, C., da Silva, J., Jeans, G., Alpers, W., & Caruso, M. (2013). Nonlinear Internal Waves in Synthetic Aperture Radar Imagery. *Oceanography*, *26*(2), 68-79. https://doi.org/10.5670/oceanog.2013.32

Jia, T., Liang, J., Li, X.-M., & Fan, K. (2019). Retrieval of internal solitary wave amplitude in shallow water by tandem spaceborne SAR. *Remote Sensing*, *11*(14), 1706. https://doi.org/https://doi.org/10.3390/rs11141706

Kao, T. W., Pan, F.-S., & Renouard, D. (1985). Internal solitons on the pycnocline: generation, propagation, and shoaling and breaking over a slope. *Journal of Fluid Mechanics*, *159*, 19-53. https://doi.org/10.1017/s0022112085003081

Lee, J. S. (1980). Digital image enhancement and noise filtering by use of local statistics. *IEEE transactions on pattern analysis and machine intelligence*, *2*, 165-168. https://doi.org/10.1109/TPAMI.1980.4766994

Li, X., Jackson, C. R., & Pichel, W. G. (2013). Internal solitary wave refraction at Dongsha Atoll, South China Sea. *Geophysical Research Letters*, *40*(12), 3128-3132. https://doi.org/10.1002/grl.50614

Liang, J., Li, X. -M., & Fan, K. (2022). Distribution and Source Sites of Nonlinear Internal Waves Northeast of Hainan Island. *Journal of Marine Science and Engineering*, *10*(1), 55. https://doi.org/10.3390/jmse10010055

Lu, K. (2024). ISWs Data of Satellite Image and Laboratory Experiments. [Dataset]. Zenodo. https://doi.org/10.5281/zenodo.10792482

Mei, Y., Wang, J., Huang, S. S., Mou, H. D., & Chen, X. (2019). Experimental investigation on the optical remote sensing images of internal solitary waves with a smooth surface. *Acta Oceanologica Sinica*, *38*(6), 124-131. https://doi.org/10.1007/s13131-019-1387-5

Melsheimer, C., & Keong, K. L. (2001). Sun glitter in spot images and the visibility of oceanic phenomena. *Proceedings of the 22nd Asian Conference on Remote Sensing*, *5*(9), 1-6. https://www.researchgate.net/publication/237686264

Meng, J., Sun, L., Zhang, H., Hu, B., Hou, F., & Bao, S. (2022). Remote sensing survey and research on internal solitary waves in the South China Sea-Western Pacific-East Indian Ocean (SCS-WPAC-EIND). *Acta Oceanologica Sinica*, *41*(10), 154-170. https://doi.org/10.1007/s13131-022-2018-0

Pan, J., Jay, D. A., & Orton, P. M. (2007). Analyses of internal solitary waves generated at the Columbia River plume front using SAR imagery. *Journal of Geophysical Research*, *112*(C7). https://doi.org/10.1029/2006jc003688

406 Quyang, Y., Chong, J., Wu, Y., & Zhu, M. (2011). Simulation studies of internal waves in SAR
407 images under different SAR and wind field conditions. *IEEE Transactions on Geoscience*
408 *and Remote Sensing*, *49*(5), 1734-1743. https://doi.org/10.1109/TGRS.2010.2087384
409 Raju, N., Dash, M. K., Dey, S. P., & Bhaskaran, P. K. (2019). Potential generation sites of
410 internal solitary waves and their propagation characteristics in the Andaman Sea—a study
411 based on MODIS true-colour and SAR observations. *Environ Monit Assess 191 (Suppl 3)*,
412 *809*, 1157-1181. https://doi.org/10.1007/s10661-019-7705-8
413 Ramp, S. R., Yang, Y. J., & Bahr, F. L. (2010). Characterizing the nonlinear internal wave
414 climate in the northeastern South China Sea. *Nonlinear Processes in Geophysics*, *17*(5),
415 481-498. https://doi.org/10.5194/npg-17-481-2010
416 Romeiser, R., & Graber, H. C. (2015). Advanced Remote Sensing of Internal Waves by
417 Spaceborne Along-Track InSAR—A Demonstration With TerraSAR-X. *IEEE*
418 *Transactions on Geoscience and Remote Sensing*, *53*(12), 6735-6751.
419 https://doi.org/10.1109/tgrs.2015.2447547
420 Schafstall, J., Dengler, M., Brandt, P., & Bange, H. (2010). Tidal-induced mixing and diapycnal
421 nutrient fluxes in the Mauritanian upwelling region. *Journal of Geophysical Research*,
422 *115*(C10), C10014-. https://doi.org/10.1029/2009jc005940
423 Shroyer, E. L., Moum, J. N., & Nash, J. D. (2010). Vertical heat flux and lateral mass transport
424 in nonlinear internal waves. *Geophysical Research Letters*, *37*(8), L08601.
425 https://doi.org/10.1029/2010gl042715
426 Sun, L., Zhang, J., & Meng, J. (2019). A study of the spatial-temporal distribution and
427 propagation characteristics of internal waves in the Andaman Sea using MODIS. *Acta*
428 *Oceanologica Sinica*, *38*(7), 121-128. https://doi.org/10.1007/s13131-019-1449-8
429 Sun, L., Zhang, J., & Meng, J. (2021). Study on the propagation velocity of internal solitary
430 waves in the Andaman Sea using Terra/Aqua-MODIS remote sensing images. *Journal of*
431 *Oceanology and Limnology*, *39*, 2195-2208. https://doi.org/10.1007/s00343-020-0280-6
432 Thielicke, W., & Stamhuis, E. J. (2014). PIVlab – Towards User-friendly, Affordable and
433 Accurate Digital Particle Image Velocimetry in MATLAB. *Journal of Open Research*
434 *Software*, *2*. https://doi.org/10.5334/jors.bl
435 Vanhellemont, Q., Neukermans, G., & Ruddick, K. (2014). Synergy between polar-orbiting and
436 geostationary sensors: Remote sensing of the ocean at high spatial and high temporal
437 resolution. *Remote Sensing of Environment*, *146*, 49-62.
438 https://doi.org/10.1016/j.rse.2013.03.035
439 Wang, J., Huang, W., Yang, J., Zhang, H., & Pan, Y. (2011). The distribution, sources, and
440 propagation of internal waves in South China Sea based on satellite remote sensing.
441 *Proceedings of SPIE - The International Society for Optical Engineering*, *8006*, 85.
442 https://doi.org/10.1117/12.902045
443 Wang, T., Huang, X., Zhao, W., Zheng, S., Yang, Y., & Tian, J. (2022). Internal Solitary Wave
444 Activities near the Indonesian Submarine Wreck Site Inferred from Satellite Images.
445 *Journal of Marine Science and Engineering*, *10*(2).
446 https://doi.org/10.3390/jmse10020197
447 Xu, J., Xie, J., Chen, Z., Cai, S., & Long, X. (2012). Enhanced mixing induced by internal
448 solitary waves in the South China Sea. *Continental Shelf Research*, *49*, 34-43.
449 https://doi.org/10.1016/j.csr.2012.09.010
450 Xu, T., Chen, X., Li, Q., He, X., Wang, J., & Meng, J. (2023). Strongly nonlinear effects on
451 determining internal solitary wave parameters from surface signatures with potential for

remote sensing applications. *Geophysical Research Letters*, *50*(23), e2023GL105814. https://doi.org/10.1029/2023GL105814

Xue, J., Graber, H. C., Lund, B., & Romeiser, R. (2013). Amplitudes Estimation of Large Internal Solitary Waves in the Mid-Atlantic Bight Using Synthetic Aperture Radar and Marine X-Band Radar Images. *IEEE Transactions on Geoscience and Remote Sensing*, *51*(6), 3250-3258. https://doi.org/10.1109/tgrs.2012.2221467

Zhang, M., Wang, J., Li, Z., Liang, K., & Chen, X. (2022). Laboratory study of the impact of the Surface Solitary Waves created by the Internal Solitary Waves on optical imaging. *Journal of Geophysical Research: Oceans*, *127*(2), e2021JC017800. https://doi.org/10.1029/2021JC017800

Zhao, Y., Liu, A. K., & Hsu, M. -K. (2008). Internal wave refraction observed from sequential satellite images. *International Journal of Remote Sensing*, *29*(21), 6381-6390. https://doi.org/10.1080/01431160802175520

Zheng, Q., Yuan, Y., Klemas, V., & Yan, X.-H. (2001). Theoretical expression for an ocean internal soliton synthetic aperture radar image and determination of the soliton characteristic half width. *Journal of Geophysical Research: Oceans*, *106*(C12), 31415-31423. https://doi.org/10.1029/2000jc000726